PAPER

The dHvA effect in Sn-doped PbTe topological crystalline insulator

To cite this article: Duncan Miertschin *et al* 2025 *J. Phys.: Condens. Matter* **37** 155501

View the article online for updates and enhancements.

The dHvA effect in Sn-doped PbTe topological crystalline insulator

Duncan Miertschin[1,7], Thinh Nguyen[1,7], Shengzhi Zhang[2], Minseong Lee[2], Sritharan Krishnamoorthi[3], Rajesh Kumar Ulaganathan[4], Raman Shankar[3], David E Graf[5,6] and Keshav Shrestha[1,*]

[1] Department of Chemistry and Physics, West Texas A & M University, 2501 4th Ave, Canyon, TX 79016, United States of America
[2] National High Magnetic Field Laboratory, Los Alamos National Laboratory, Los Alamos, NM 87545, United States of America
[3] Institute of Physics, Academia Sinica, Nankang, Taipei 11529, Taiwan, Republic of China
[4] Centre for Nanotechnology, Indian Institute of Technology Roorkee, Roorkee 247667, India
[5] National High Magnetic Field Laboratory, Tallahassee, FL 32310, United States of America
[6] Department of Physics, Florida State University, Tallahassee, FL 32306, United States of America

E-mail: kshrestha@wtamu.edu and drkeshavshrestha@gmail.com

CrossMark

Abstract

We report the synthesis, electrical transport, magnetotransport, and high-field torque magnetometry studies of the topological crystalline insulator $Sn_xPb_{1-x}Te$ ($x = 0$, 0.2, and 0.4). This material undergoes a topological phase transition from trivial to non-trivial at a critical doping of $x_c = 0.35$. The resistivity increases with applied magnetic field, displaying positive magnetoresistance (MR), which reaches up to 4500% at 14 T for PbTe. However, we did not observe Shubnikov–de Haas oscillations in the MR data. To observe quantum oscillations and explore the Fermi surface topology of this material, we conducted torque magnetometry experiments on samples both below ($x = 0.2$) and above ($x = 0.4$) the critical doping $x_c = 0.35$ with applied magnetic fields up to 35 T. The torque signal from both samples revealed clear de Haas–van Alphen (dHvA) oscillations above 15 T. These oscillations exhibited single dominant frequencies of 90 T for $x = 0.2$ and 51 T for $x = 0.4$, providing insights into the Fermi surface properties. Angular and temperature-dependent analyses of the dHvA oscillations were performed using Lifshitz–Kosevich theory to extract key physical parameters of the Fermi surface. Berry phase analysis based on Landau level fan diagrams revealed non-zero values for both $x = 0.2$ and $x = 0.4$, indicating non-trivial topological features. This study provides detailed insights into the quantum oscillations and Fermi surface properties of Sn-doped PbTe/Se compounds, contributing to a deeper understanding of topological crystalline materials and their broader implications for topological physics.

Keywords: torque magnetometry, Fermi surface, de Haas–van Alphen effect

---

[7] Equal contribution.
[*] Author to whom any correspondence should be addressed.

1. Introduction

Topological insulators (TIs) have garnered substantial attention since their discovery due to their unique electronic properties and potential applications in advanced technologies, such as spintronics and low-power electronics [1–4]. These materials are characterized by an insulating bulk and highly conducting surface states, which arise from the non-trivial topology of the bulk electronic states. The surface states of TIs are protected by time-reversal symmetry, which makes them robust against non-magnetic impurities and scattering [1]. TIs were initially predicted theoretically in materials with strong spin–orbit coupling and later experimentally verified in Bi–Se–Te systems [5–8], commonly known as 3D TIs. The investigation and confirmation of TI properties rely on a variety of experimental techniques, including angle-resolved photoemission spectroscopy (ARPES) [7], weak antilocalization (WAL) [9–11], and quantum oscillations [6, 12–22]. Among these, quantum oscillations, such as de Haas–van Alphen (dHvA) oscillations, are particularly easier and valuable for probing the electronic properties of TIs. Measuring torque under high magnetic fields allows the observation of dHvA oscillations, which provide detailed insights into the Fermi surface, effective mass, and other critical electronic parameters of the material [1].

Among the various types of TIs, a notable subclass is the topological crystalline insulators (TCIs) [23]. TCIs differ from conventional TIs in that their topological surface states are protected by crystal symmetries, such as mirror symmetry, rather than time-reversal symmetry [24, 25]. These materials, often exhibiting a simple rock salt crystal structure, include elements from groups IV and VI. TCIs are characterized by semiconducting bulk states, metallic gapless surface states, and an even number of Dirac cones at certain surface terminations [26–28].

The compound $Sn_xPb_{1-x}Te$/Se is known to exhibit TCI features, as confirmed by both theoretical and experimental studies [24, 25, 27]. It is found that this material changes topological properties either by doping or external pressure, making them an ideal platform for studying topological phase transitions [29–31]. In this system, increasing the Sn content induces band inversion at critical doping levels, with $x_c = 0.17$ for $Sn_xPb_{1-x}Se$ [27] and $x_c = 0.35$ for $Sn_xPb_{1-x}Te$ [32]. At and above these critical doping levels, the system transitions to a topologically non-trivial phase. These transitions have been explored using techniques such as ARPES and WAL. However, quantum oscillation studies [18, 33–40] have primarily focused on the parent compounds PbTe and SnTe, despite their potential to offer detailed insights into the topological properties of materials.

In this study, we synthesized high-quality single crystals of $Sn_xPb_{1-x}Te$ ($x = 0$, 0.2, and 0.4) and carried out detailed Fermi surface studies on samples both below ($x = 0.2$) and above ($x = 0.4$) the critical doping using torque magnetometry with applied magnetic fields up to 35 T and temperatures as low as 0.35 K. Our torque measurements revealed

clear and well-defined dHvA oscillations with a single dominant frequency. The angular and temperature dependence of the dHvA oscillations was analyzed to extract key parameters of the Fermi surface.

2. Experimental details

Single crystals of $Sn_xPb_{1-x}Te$ were grown by the chemical vapor transport method. High-purity (99.9999%) lead, tin, and tellurium were used in the crystal growth. Initially, high-purity powders of PbTe (62 atomic % Pb and 38 atomic % Te) and SnTe (48 atomic % Sn and 52 atomic % Te) were prepared via solid-state reaction. The nominal concentrations of the mixture were estimated based on the Pb:Sn weight ratio. The mixture was heated in a clean evacuated quartz tube to 900 °C and held at this temperature for 48 h before proceeding with crystal growth. Subsequently, the powders were sealed in evacuated quartz tubes with dimensions of $2.2 \times 2 \times 40 \, cm^3$, along with ∼150 mg of iodine (I_2) as the transport agent. The sealed tubes were placed in a horizontal two-zone furnace for 10 d at 900 °C–800 °C and then gradually cooled to room temperature.

High-field measurements were conducted at the National High Magnetic Field Laboratory (NHMFL) in Tallahassee, Florida, with a maximum applied field of 35 T in a DC resistive water-cooled magnet, using a top-loaded ^{3}He cryostat. Electrical resistance was measured using the standard four-probe method, while torque (τ) was measured with the piezoresistive cantilever method. The sample was rotated *in-situ* within the applied magnetic fields at various tilt angles (θ), where θ is the angle between the magnetic field and the c-axis of the sample, as shown in figure 2(a) inset. Magnetic fields were swept at each fixed temperature at a rate of 2 T min^{-1}.

3. Results and discussion

Figure 1(a) shows the x-ray diffraction (XRD) data for $Sn_xPb_{1-x}Te$ samples ($x = 0$, 0.2, and 0.4) measured at room temperature. For simplicity, we refer to the $x = 0.2$ and $x = 0.4$ samples as Sn0.2 and Sn0.4, respectively. PbTe crystallizes in a cubic structure. Upon doping with Sn at the Pb site, the XRD peak shifts to the right, as observed for the (200) peak in the inset. This shift indicates that the lattice parameter decreases as Pb is replaced with Sn. Our previous doping-dependent XRD data [36] demonstrate that the lattice parameter decreases linearly with increasing Sn content in $Sn_xPb_{1-x}Te$. To investigate the electrical properties of these compounds, we measured their electrical resistance as a function of temperature down to 2 K, as shown in figure 1(b). The electrical resistance decreases while decreasing temperature for all samples, indicating their metallic behavior. The inset shows the magnetoresistance (MR) data, defined as MR $= [R_{xx}(H) - R_{xx}(0)]/R_{xx}(0)$, where $R_{xx}(H)$ and $R_{xx}(0)$ represent the resistivity value at H field and 0 T, respectively. All the samples exhibit positive MR, with the value reaching 4500%, 63%, and 130% for
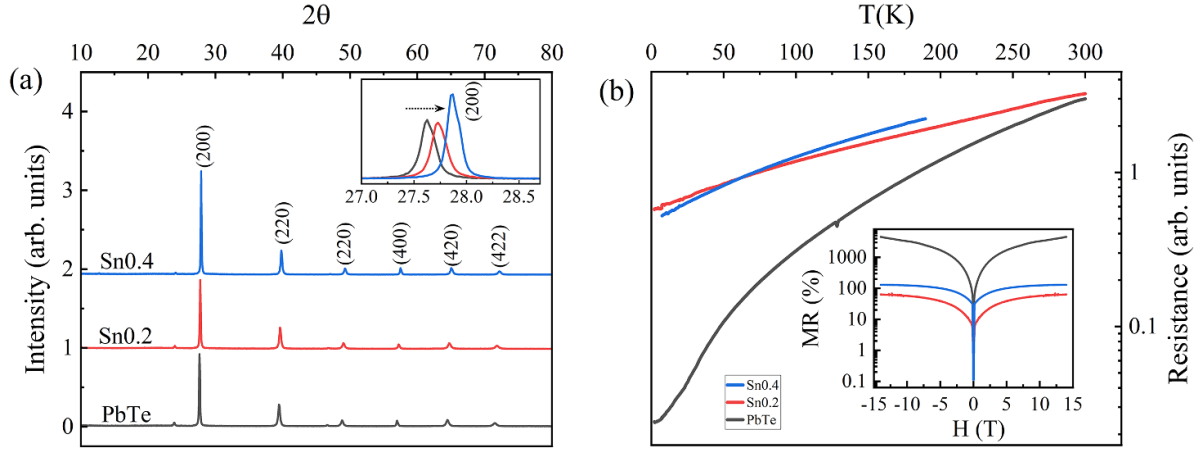
Figure 1. (a) Room-temperature x-ray diffraction data for $Sn_xPb_{1-x}Te$ samples. The graph is shifted vertically for clarity. Inset: a zoomed-in view of the (200) peak, which shifts to the right at higher *x*. (b) Resistivity versus temperature plots for $Sn_xPb_{1-x}Te$ samples. Inset: magnetoresistance (MR) plots for $Sn_xPb_{1-x}Te$ samples, showing that PbTe has the maximum MR value of ∼4500%. The *y*-axis is in logarithmic scale for clarity.

PbTe, Sn0.2, and Sn0.4, respectively. The features of metallic behavior and positive MR of the same order have also been observed in previous electrical and magnetotransport measurements [33, 36, 41]. For example, Ma *et al* [33] reported a MR of ∼4200% under 14 T for PbTe at 2 K. However, unlike previous studies [33–38, 42, 43], we did not observe any signs of Shubnikov–de Haas (SdH) oscillations in the MR data for any of the samples. Therefore, we employed torque magnetometry to probe the Fermi surface properties of these compounds.

Figure 2(a) shows the torque data for Sn0.2 and Sn0.4 samples with the maximum applied field of 35 T. As seen in the graph, the torque signal shows clear dHvA oscillations above 15 T. The oscillation is smooth and well defined and observed in both samples. We carried out torque measurement at different temperature. Figure 2(b) shows the dHvA oscillations after the background subtraction for Sn0.2 and Sn0.4 samples. As expected, the amplitude of the dHvA oscillations decreases at higher temperatures. It is important to note that the oscillations survive even temperature is increased to 60 K, indicating the high quality of our samples.

We have carried the frequency analyses of dHvA oscillations observed here. Figure 2(c) displays the frequency spectrum of the quantum oscillations data shown in figure 2(b). As expected, there is one major frequency peak at 90 T and 51 T for Sn0.2 and Sn0.4, respectively and the amplitude of the frequency peak decreases at higher temperatures. It appears that the frequency of quantum oscillations decreases while increasing the Sn-doping. According to Onsager's relation [1, 44, 45], the frequency (*F*) of quantum oscillation is directly proportional to the cross-section area of the Fermi surface as $F = \hbar/(2\pi e)A_F^2$, where $\hbar$ is reduced Planck's constant and *e* is the charge of an electron. Therefore, the quantum oscillation frequency is the direct measure of the Fermi surface of the material under study. The decrease of frequency at higher Sn concentration implies that the cross-section area of the Fermi surface decreases.

As seen in figure 2(b), the amplitude of the oscillations decreases at higher temperatures. This behavior can be described by the Lifshitz–Kosevich (LK) theory [44]. According to the LK theory, the temperature and magnetic field dependence of quantum oscillations in torque are given by

$$\Delta\tau(T,H) \propto e^{-\lambda_D}\frac{\lambda(T/H)}{\sinh[\lambda(T/H)]}, \tag{1}$$

with $\lambda_D(H) = \frac{2\pi^2 k_B}{\hbar e}m^*\frac{T_D}{H}$ and $\lambda(T/H) = \frac{2\pi^2 k_B}{\hbar e}m^*\frac{T}{H}$. Here, T_D, k_B and m^* represent the Dingle temperature, Boltzmann's constant, and effective mass of the charge carriers, respectively. The first term is the Dingle factor, which describes the attenuation of the oscillations with decreasing field *H*. The second term explains the weakening of the oscillations at higher temperatures.

Figure 2(d) presents the variation of frequency amplitude with temperature for Sn0.2 and Sn0.4, represented by scattered circles and solid squares, respectively. The solid curves correspond to the best-fit results obtained using the temperature dependent term in the LK theory (1). As evident from the graph, the LK formula describes the temperature-dependent data of Sn0.2 and Sn0.4. From the best-fit parameters, the effective mass was estimated to be $m^* = 0.095m_o$ and $0.079m_o$ for Sn0.2 and Sn0.4, respectively, where m_o is the free mass of an electron. To determine additional physical parameters of the charge carriers, we carried out the Dingle temperature analyses by fitting the field dependence of the magnetic field, as shown in the inset. Our analysis yielded $T_D = 11.5$ K and 0.4 K for Sn0.2 and Sn0.4, respectively. It is important to note that our $T_D = 11.5$ K for Sn0.2 is in good agreement with 10.2 K reported for PbTe single crystal [33], however, it is nearly four times smaller than the value reported ($T_D = 46$ K) for SnTe thin film [34]. As T_D is the measure of disorder and impurity scattering in material. The smaller T_D values in our samples
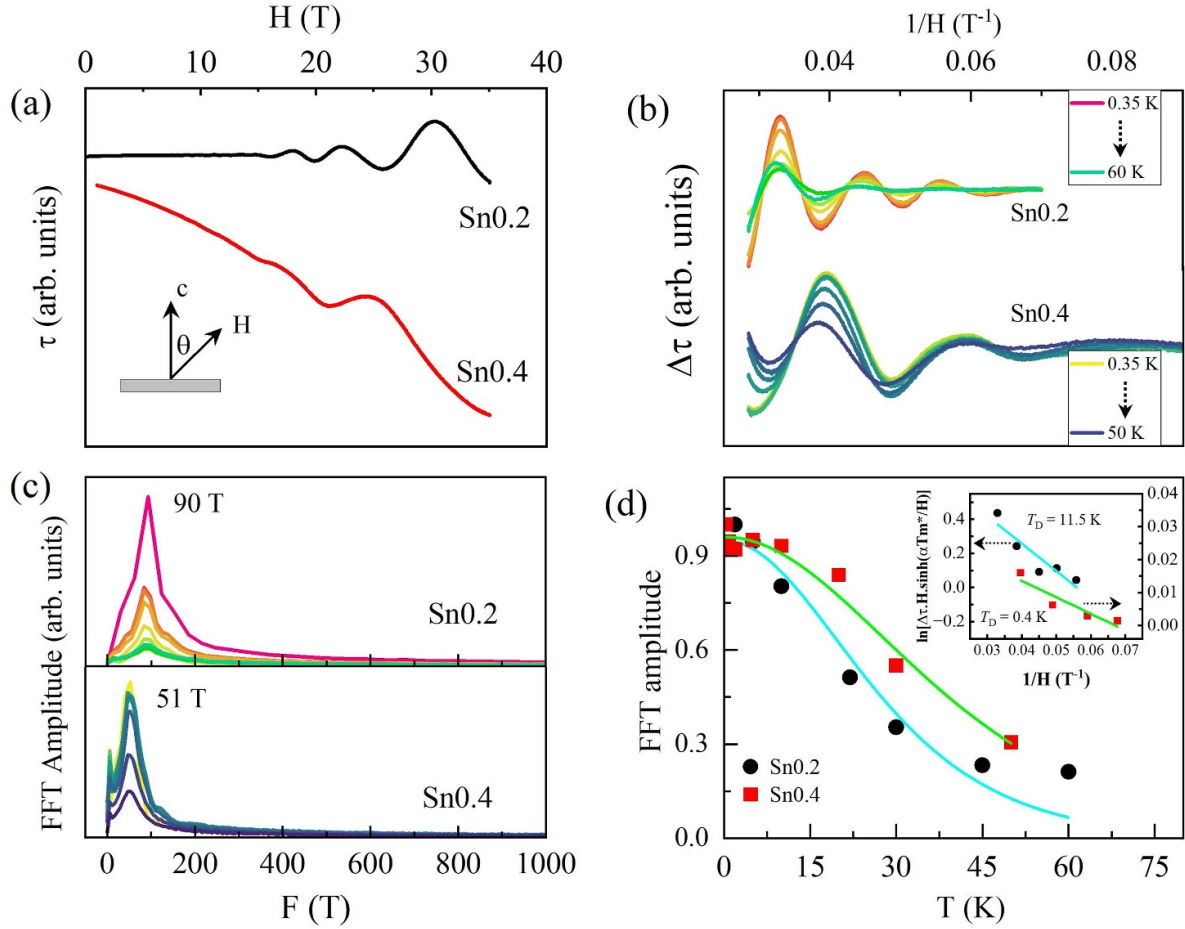
Figure 2. (a) Torque data for $Sn_xPb_{1-x}Te$ with $x = 0.2$ (Sn0.2) and $x = 0.4$ (Sn0.4), measured at $\theta = 20°$ and $\theta = 0°$, respectively. The signal shows clear de Haas–van Alphen (dHvA) oscillations above 15 T. Inset: a schematic diagram showing the tilt angle θ. (b) The dHvA oscillations of Sn0.2 and Sn0.4 at different temperatures, measured at tilt angles of $\theta = 20°$ and $0°$, respectively. The amplitude of the oscillations decreases at higher temperatures. (c) Frequency spectrum of the dHvA oscillations shown in (b). A single frequency is observed at 90 T and 51 T for Sn0.2 and Sn0.4, respectively. (d) Variation of frequency amplitude with temperature for Sn0.2 and Sn0.4 samples. The solid curves represent the best fits to the data obtained using the Lifshitz–Kosevich formula. Inset: dingle plot for both samples.

Table 1. Physical parameters: frequency (F), Fermi wave vector (k_F), effective mass (m^*), Fermi velocity (v_F), Dingle temperature (T_D), quantum relaxation time (τ_s), mean free path (ℓ_{2D}), quantum mobility (μ), and Berry phase (Φ_B).

| Sample	F (T)	m^*/m_o	T_D (K)	v_F (m s^{-1})	τ (ps)	ℓ_{2D} (nm)	μ (m^2 V^{-1} s^{-1})	Φ_B (π)
Sn0.2	90	0.095	11.5	6.24	0.1	6.57	0.2	0.64 ± 0.12
Sn0.4	51	0.079	0.4	5.80	3	175.55	6.7	0.40 ± 0.01

indicate high purity of Sn0.2 and Sn0.4 samples. The observation of dHvA oscillations even above 50 K (figure 2) in Sn0.2 and Sn0.4 is indication of their high quality and consistent with lower T_D values.

Using the values of m_o and T_D, we estimated several physical parameters for the charge carriers: the Fermi velocity (v_F), scattering time (τ), mean free path (ℓ_{2D}), and quantum mobility (μ). The Fermi surface parameters for Sn0.2 and Sn0.4 are tabulated in table 1. As seen in the table, Sn0.4 has a smaller T_D and consequently exhibits significantly larger τ, ℓ_{2D}, and μ values compared to those of Sn0.2.

The frequency of the dHvA oscillations is directly proportional to the cross-sectional area of the Fermi surface, as

described by Onsager's relation [1, 44, 45]. By rotating the sample in a magnetic field, it is possible to map the Fermi surface of the material under study. To this end, we conducted angular-dependent torque measurements for Sn0.2 and Sn0.4, as shown in figures 3(a) and (b), respectively. As illustrated in the graphs, quantum oscillations are observed at all tilt angles, including when the magnetic field is parallel to the sample surface ($\theta = 90°$). This observation indicates that the Fermi surfaces of these materials are three-dimensional. The period of the oscillations changes with varying θ, suggesting a corresponding variation in frequency. To analyze the angular dependence of the frequency, we subtracted a smooth polynomial background from the data and performed a Fourier
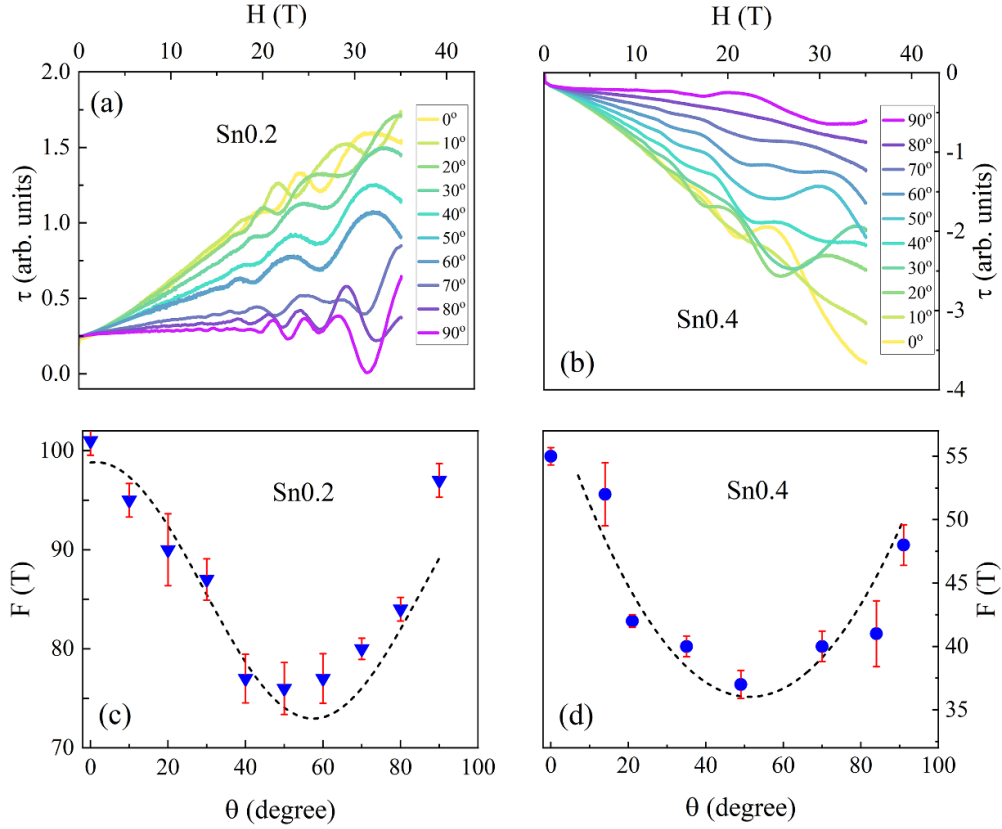
Figure 3. Angle dependent torque data for $Sn_xPb_{1-x}Te$ with (a) $x = 0.2$ (Sn0.2) and (b) $x = 0.4$ (Sn0.4). The de Haas–van Alphen (dHvA) oscillations are clearly observed in both samples at all tilt angles θ. The frequency decreases with increasing θ values for (c) Sn0.2 and (d) Sn0.4 samples. The dashed curves serve as guides to the eye.

transform. Figures 3(c) and (d) display the dHvA frequency variation with θ for Sn0.2 and Sn0.4, respectively. For both samples, the frequency initially decreases up to $\theta = 50°$ and then increases with further increases in θ, as indicated by the dashed curves. This angular dependence is consistent with SdH oscillation studies [46] on the parent compound PbTe.

To analyze the topological properties of Sn0.2 and Sn0.4, we estimated the Berry phase (Φ_B) by constructing a Landau level (LL) fan diagram. For topologically trivial systems, $\Phi_B = 0$, while for topologically non-trivial systems, $\Phi_B = \pi$ [1]. The torque exerted on the system is expressed as $\vec{\tau} = V\mu_0 \vec{H} \times \vec{M} = V\mu_0 HM \sin\beta$, where V is the sample volume, μ_0 is the permeability of free space, and β is the angle between $\vec{M}$ and $\vec{H}$. Assuming $\beta = 90°$, the component of magnetization perpendicular to the external field can be extracted from the torque data. Figure 4(a) shows the perpendicular component of magnetization after background subtraction for Sn0.2 and Sn0.4, clearly revealing dHvA oscillations in both samples. We constructed the LL fan diagram by assigning $(N - \frac{1}{4})$ to the minima and $(N + \frac{1}{4})$ to the maxima of the oscillation, where N is the LL index [1, 47–49]. The resulting LL fan plot is presented in figure 4(b). To extract the Φ_B, we carried out the linear extrapolation to the limit $1/H \to 0$, which yields intercepts of $N_0 = 0.32$ and 0.20 for Sn0.2 and Sn0.4, respectively. These intercepts correspond to Berry phase values of $\Phi_B = (0.64 \pm 0.12)\pi$ for Sn0.2 and $\Phi_B = (0.40 \pm 0.01)\pi$ for Sn0.4.

The non-zero Φ_B values indicate that both samples exhibit non-trivial topological properties [1, 50–55]. From the linear interpolation, the slope value was found to be (87.99 ± 1.37) T and (52.14 ± 0.11) T, which are in good agreement with the frequency values of 88 T and 51 T for Sn0.2 and Sn0.4, respectively, as shown in figure 2(c). This eventually provides additional support for the reliability of Φ_B calculations using the LL fan plot.

4. Summary

In this work, we synthesized and characterized $Sn_xPb_{1-x}Te$ ($x = 0, 0.2,$ and 0.4) using electrical transport, magnetoresistance (MR), and torque magnetometry under magnetic fields of up to 35 T. All three samples exhibited metallic behavior, with MR reaching as high as 4500% under 14 T for PbTe. While no SdH oscillations were observed in the MR signal, clear dHvA oscillations were detected in the torque signal up to 35 T. For the $x = 0.2$ (Sn0.2) and $x = 0.4$ (Sn0.4) samples, we identified dominant oscillation frequencies of 90 T and 51 T, respectively. The frequency of quantum oscillation is directly proportional to the cross-sectional area of the Fermi surface. The presence of a single frequency peak in the dHvA oscillation strongly indicates that both Sn0.2 and Sn0.4 possess a single Fermi surface pocket. Furthermore, angle-dependent torque measurements revealed the persistence of dHvA oscillations even
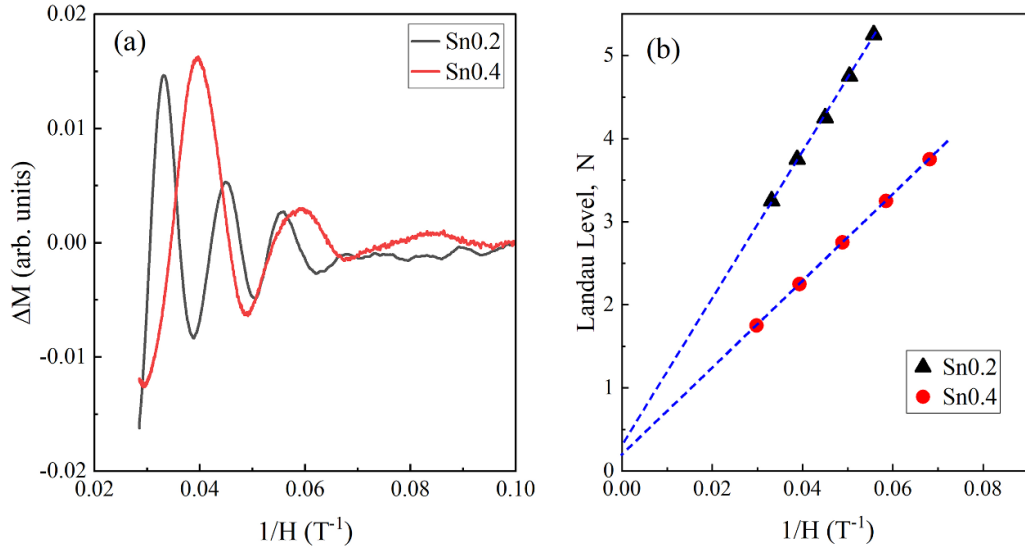
Figure 4. (a) Background-subtracted magnetization data for $Sn_xPb_{1-x}Te$ with (a) $x = 0.2$ (Sn0.2) and (b) $x = 0.4$ (Sn0.4). (b) The Landau level fan diagram constructed by assigning $(N + 1/4)$ and $(N - 1/4)$ for maxima and minima in quantum oscillations, respectively. The dashed lines represent the linear extrapolation of the data as $1/H$ approaches 0.

when the magnetic field was aligned parallel to the sample surface, confirming the presence of three-dimensional Fermi surface pockets in these materials.

To explore the topological properties of Sn0.2 and Sn0.4, we constructed LL fan plots and determined the Berry phases as $\Phi_\mathbf{B} = (0.64 \pm 0.12)\pi$ and $\Phi_\mathbf{B} = (0.40 \pm 0.01)\pi$, respectively. Since $\Phi_\mathbf{B} = 0$ (or π) is indicative of a topologically trivial (or non-trivial) system [1, 56], the non-zero values observed suggest that the properties of Sn0.2 and Sn0.4 are influenced by non-trivial topology. $Sn_xPb_{1-x}Te$ undergoes a topological phase transition from trivial to non-trivial at a critical doping of $x_c = 0.35$ [32]. Our Berry phase calculations reveal values of 0.62π for Sn0.2 and 0.40π for Sn0.4. While these results suggest a slight decrease in the Berry phase, both values remain non-zero and are not close to π. This indicates that the critical doping value x_c might be higher than the previously predicted value of 0.35. To determine x_c more precisely, systematic studies of the doping dependence are required. Although $\Phi_\mathbf{B}$ is slightly smaller for Sn0.4 compared to Sn0.2, the higher mean free path of charge carriers and greater mobility values (table 1) indicate a stronger influence of non-trivial topological features in Sn0.4 than in Sn0.2. Our studies show that a doping level farther from x_c may be required to fully observe quantum transport properties dominated by non-trivial topology in $Sn_xPb_{1-x}Te$. The detailed analysis of electrical and magnetic properties under extreme magnetic fields presented in this work provides valuable insights into the electronic structure of $Sn_xPb_{1-x}Te/Se$, advancing the broader understanding of topological crystalline materials and other topological systems.

Data availability statement

All data that support the findings of this study are included within the article (and any supplementary files).

ORCID iDs

Shengzhi Zhang ⓘ https://orcid.org/0000-0002-1076-6662
Minseong Lee ⓘ https://orcid.org/0000-0002-2369-9913
Rajesh Kumar Ulaganathan ⓘ https://orcid.org/0000-0001-8886-6332
Raman Shankar ⓘ https://orcid.org/0000-0003-4702-2517
Keshav Shrestha ⓘ https://orcid.org/0000-0001-7786-3611

References

[1] Ando Y 2013 Topological insulator materials *J. Phys. Soc. Japan* **82** 102001
[2] Hasan M Z and Kane C L 2010 *Colloquium*: Topological insulators *Rev. Mod. Phys.* **82** 3045

[3] Qi X-L and Zhang S-C 2011 Topological insulators and superconductors *Rev. Mod. Phys.* **83** 1057

[4] Moore J E 2010 The birth of topological insulators *Nature* **464** 194

[5] Shrestha K, Chou M, Graf D, Yang H, Lorenz B and Chu C 2017 Extremely large nonsaturating magnetoresistance and ultrahigh mobility due to topological surface states in the metallic Bi_2Te_3 topological insulator *Phys. Rev.* B **95** 195113

[6] Taskin A, Ren Z, Sasaki S, Segawa K and Ando Y 2011 Observation of Dirac holes and electrons in a topological insulator *Phys. Rev. Lett.* **107** 016801

[7] Chen Y *et al* 2009 Experimental realization of a three-dimensional topological insulator, Bi_2Te_3 *Science* **325** 178

[8] Xia Y *et al* 2009 Observation of a large-gap topological-insulator class with a single Dirac cone on the surface *Nat. Phys.* **5** 398

[9] Shrestha K, Graf D, Marinova V, Lorenz B and Chu C 2017 Weak antilocalization effect due to topological surface states in $Bi_2Se_{2.1}Te_{0.9}$ *J. Appl. Phys.* **122** 145901

[10] He H-T, Wang G, Zhang T, Sou I-K, Wong G K L, Wang J-N, Lu H-Z, Shen S-Q and Zhang F-C 2011 Impurity effect on weak antilocalization in the topological insulator Bi_2Te_3 *Phys. Rev. Lett.* **106** 166805

[11] Bao L *et al* 2012 Weak anti-localization and quantum oscillations of surface states in topological insulator Bi_2Se_2Te *Sci. Rep.* **2** 726

[12] Shrestha K, Marinova V, Lorenz B and Chu C 2018 Evidence of a 2D Fermi surface due to surface states in a *p*-type metallic Bi_2Te_3 *J. Phys.: Condens. Matter* **30** 185601

[13] Shrestha K, Marinova V, Lorenz B and Chu P C 2014 Shubnikov–de Haas oscillations from topological surface states of metallic $Bi_2Se_{2.1}Te_{0.9}$ *Phys. Rev.* B **90** 241111

[14] de Castro S, Abramof E, Rappl P and Peres M 2024 Detection of Dirac fermions in capped snte film via magnetotransport measurements *J. Appl. Phys.* **135** 205701

[15] Shrestha K, Marinova V, Graf D, Lorenz B and Chu C W 2017 Quantum oscillations in metallic $SbTe_2Se$ topological insulator *Phys. Rev.* B **95** 075102

[16] Xiong J, Petersen A C, Qu D, Hor Y S, Cava R J and Ong N P 2012 Quantum oscillations in a topological insulator Bi_2Te_2Se with large bulk resistivity (6 Ω cm) *Physica* E **44** 917

[17] Shrestha K, Graf D E, Marinova V, Lorenz B and Chu P C 2017 Simultaneous detection of quantum oscillations from bulk and topological surface states in metallic $Bi_2Se_{2.1}Te_{0.9}$ *Phil. Mag.* **97** 1740

[18] O'Neill C D, Clark O J, Keen H D, Mazzola F, Marković I, Sokolov D A, Malekos A, King P D, Hermann A and Huxley A D 2020 Changes of Fermi surface topology due to the rhombohedral distortion in SnTe *Phys. Rev.* B **102** 155132

[19] Qu D-X, Hor Y S, Xiong J, Cava R J and Ong N P 2010 Quantum oscillations and Hall anomaly of surface states in the topological insulator Bi_2Te_3 *Science* **329** 821

[20] Lawson B J, Hor Y and Li L 2012 Quantum oscillations in the topological superconductor candidate $Cu_{0.25}Bi_2Se_3$ *Phys. Rev. Lett.* **109** 226406

[21] Taskin A, Yang F, Sasaki S, Segawa K and Ando Y 2014 Topological surface transport in epitaxial SnTe thin films grown on Bi_2Te_3 *Phys. Rev.* B **89** 121302

[22] Shrestha K, Marinova V, Graf D, Lorenz B and Chu C 2017 Large magnetoresistance and Fermi surface study of $SbSe_2Te$ single crystal *J. Appl. Phys.* **122** 125901

[23] Hsieh T H, Lin H, Liu J, Duan W, Bansil A and Fu L 2012 Topological crystalline insulators in the SnTe material class *Nat. Commun.* **3** 982

[24] Fu L 2011 Topological crystalline insulators *Phys. Rev. Lett.* **106** 106802

[25] Tanaka Y, Ren Z, Sato T, Nakayama K, Souma S, Takahashi T, Segawa K and Ando Y 2012 Experimental realization of a topological crystalline insulator in SnTe *Nat. Phys.* **8** 800

[26] Dziawa P *et al* 2012 Topological crystalline insulator states in $Pb_{1-x}Sn_xSe$ *Nat. Mater.* **11** 1023

[27] Xu S-Y *et al* 2012 Observation of a topological crystalline insulator phase and topological phase transition in $Pb_{1-x}Sn_xTe$ *Nat. Commun.* **3** 1192

[28] Tanaka Y, Sato T, Nakayama K, Souma S, Takahashi T, Ren Z, Novak M, Segawa K and Ando Y 2013 Tunability of the k-space location of the Dirac cones in the topological crystalline insulator $Pb_{1-x}Sn_xTe$ *Phys. Rev.* B **87** 155105

[29] Zhang C-L, Liang T, Ogawa N, Kaneko Y, Kriener M, Nakajima T, Taguchi Y and Tokura Y 2020 Highly tunable topological system based on PbTe-SnTe binary alloy *Phys. Rev. Mater.* **4** 091201

[30] Yan C *et al* 2014 Experimental observation of Dirac-like surface states and topological phase transition in $Pb_{1-x}Sn_xTe$ (111) films *Phys. Rev. Lett.* **112** 186801

[31] Liang T, Kushwaha S, Kim J, Gibson Q, Lin J, Kioussis N, Cava R J and Ong N P 2017 A pressure-induced topological phase with large berry curvature in $Pb_{1-x}Sn_xTe$ *Sci. Adv.* **3** e1602510

[32] Zeljkovic I *et al* 2015 Dirac mass generation from crystal symmetry breaking on the surfaces of topological crystalline insulators *Nat. Mater.* **14** 318

[33] Ma S, Guo C, Xiao C, Wu F, Smidman M, Lu Y, Yuan H and Wu H 2018 Realization of a new topological crystalline insulator and Lifshitz transition in PbTe *Adv. Funct. Mater.* **28** 1803188

[34] Okazaki A, Wiedmann S, Pezzini S, Peres M, Rappl P and Abramof E 2018 Shubnikov–de haas oscillations in topological crystalline insulator SnTe (111) epitaxial films *Phys. Rev.* B **98** 195136

[35] Akiba K, Miyake A, Sakai H, Katayama K, Murakawa H, Hanasaki N, Takaoka S, Nakanishi Y, Yoshizawa M and Tokunaga M 2018 Quantitative evaluation of Dirac physics in PbTe *Phys. Rev.* B **98** 115144

[36] Shrestha K, Miertschin D, Sankar R, Lorenz B and Chu C 2021 Large magnetoresistance and quantum oscillations in $Sn_{0.05}Pb_{0.95}Te$ *J. Phys.: Condens. Matter* **33** 335501

[37] Dybko K, Szot M, Szczerbakow A, Gutowska M, Zajarniuk T, Domagala J, Szewczyk A, Story T and Zawadzki W 2017 Experimental evidence for topological surface states wrapping around a bulk SnTe crystal *Phys. Rev.* B **96** 205129

[38] Zhang B *et al* 2015 Quantum oscillations in a two-dimensional electron gas at the rocksalt/zincblende interface of PbTe/CdTe (111) heterostructures *Nano Lett.* **15** 4381

[39] Thompson T, Aron P R, Chandrasekhar B and Langenberg D 1971 Magnetostriction and magnetoelastic quantum oscillations in *p*-PbTe *Phys. Rev.* B **4** 518

[40] Bolaños K, de Castro S, Rappl P, Abramof E and Peres M 2022 Light-induced Shubnikov–de Haas oscillations and evidence of Dirac fermions in *n*-type PbTe single quantum well *Physica* E **144** 115458

[41] Roychowdhury S, Ghara S, Guin S N, Sundaresan A and Biswas K 2016 Large linear magnetoresistance in topological crystalline insulator $Pb_{0.6}Sn_{0.4}Te$ *J. Solid State Chem.* **233** 199

[42] Pena F, Wiedmann S, Abramof E, Soares D, Rappl P, de Castro S and Peres M 2021 Quantum Hall effect and Shubnikov–de Haas oscillations in a high-mobility p-type PbTe quantum well *Phys. Rev.* B **103** 205305

[43] Costa I, Mengui U, Abramof E, Rappl P, Soares D, de Castro S and Peres M 2021 Investigation of Shubnikov–de Haas

oscillations in a crystalline topological insulator SnTe/Sn$_{1-x}$Eu$_x$Te heterostructure *Phys. Rev.* B **104** 125203

[44] Shoenberg D 2009 *Magnetic Oscillations in Metals* (Cambridge University Press)

[45] Kittel C and McEuen P 2018 *Introduction to Solid State Physics* (Wiley)

[46] Jensen J, Houston B and Burke J 1978 Fermi-surface parameters of *p*-type PbTe as a function of carrier density *Phys. Rev.* B **18** 5567

[47] Nguyen T, Aryal N, Pokharel B K, Harnagea L, Mierstchin D, Popović D, Graf D and Shrestha K 2022 Fermiology of the Dirac type-II semimetal candidates (Ni, Zr)Te$_2$ using de Haas–van Alphen oscillations *Phys. Rev.* B **106** 075154

[48] Shrestha K *et al* 2022 Nontrivial Fermi surface topology of the kagome superconductor CsV$_3$Sb$_5$ probed by de Haas–van Alphen oscillations *Phys. Rev.* B **105** 024508

[49] Zheng W, Schönemann R, Mozaffari S, Chiu Y-C, Goraum Z B, Aryal N, Manousakis E, Siegrist T M, Wei K and Balicas L 2020 Bulk Fermi surfaces of the Dirac type-II semimetallic candidate NiTe$_2$ *Phys. Rev.* B **102** 125103

[50] Shrestha K *et al* 2023 High quantum oscillation frequencies and nontrivial topology in kagome superconductor KV$_3$Sb$_5$ probed by torque magnetometry up to 45 T *Phys. Rev.* B **107** 155128

[51] Chapai R, Reddy P S, Xing L, Graf D E, Karki A B, Chang T-R and Jin R 2023 Evidence for unconventional superconductivity and nontrivial topology in PdTe *Sci. Rep.* **13** 6824

[52] Shrestha K, Shi M, Nguyen T, Miertschin D, Fan K, Deng L, Graf D E, Chen X and Chu C-W 2023 Fermi surface mapping of the kagome superconductor RbV$_3$Sb$_5$ using de Haas–van Alphen oscillations *Phys. Rev.* B **107** 075120

[53] Amit, Singh R K, Wadehra N, Chakraverty S and Singh Y 2018 Type-II Dirac semimetal candidates ATe$_2$ (A = Pt, Pd): a de Haas–van Alphen study *Phys. Rev. Mater.* **2** 114202

[54] Shrestha K, Regmi B, Pokharel G, Kim S-G, Wilson S D, Graf D E, Magar B A, Phillips C and Nguyen T 2023 Electronic properties of kagome metal ScV$_6$Sn$_6$ using high-field torque magnetometry *Phys. Rev.* B **108** 245119

[55] Singha R, Pariari A K, Satpati B and Mandal P 2017 Large nonsaturating magnetoresistance and signature of nondegenerate Dirac nodes in ZrSiS *Proc. Natl Acad. Sci.* **114** 2468

[56] Miertschin D, Nguyen T, Bhandari S R, Shtefiienko K, Phillips C, Magar B A, Sankar R, Graf D E and Shrestha K 2024 Anisotropic quantum transport in ZrSiS probed by high-field torque magnetometry *Phys. Rev.* B **110** 085140